Graphene formation mechanisms on 4*H*-SiC(0001)

Michael L. Bolen,[1,2,*] Sara E. Harrison,[1,2] Laura B. Biedermann,[3,2,†] and Michael A. Capano[1,2]
[1]*School of Electrical Engineering, Purdue University, West Lafayette, Indiana 47907, USA*
[2]*Birck Nanotechnology Center, Purdue University, West Lafayette, Indiana 47907, USA*
[3]*Department of Physics, Purdue University, West Lafayette, Indiana 47907, USA*
(Received 6 May 2009; revised manuscript received 27 August 2009; published 25 September 2009)

Graphene is created through thermal decomposition of the Si face of 4*H*-SiC in high-vacuum. Growth temperature and time are varied independently to gain a better understanding of how surface features and morphology affect graphene formation. Growth mechanisms of graphene are studied by *ex situ* atomic force microscopy (AFM) and scanning tunneling microscopy (STM). On the route toward a continuous graphene film, various growth features, such as macroscale step bunching, terrace pits, and fingers, are found and analyzed. Topographic and phase AFM analysis demonstrates how surface morphology changes with experimental conditions. Step-bunched terraces and terrace pits show a strong preference for eroding along the $\{11\bar{2}0\}$ planes. Data from AFM are corroborated with STM to determine the surface structure of the growth features. It is shown that elevated finger structures are SiC while the depressed interdigitated areas between the fingers are comprised of at least a monolayer of graphene. Graphene formation at the bottom of terrace pits shows a dependence on pit depth. These features lend support for a stoichiometric view of graphene formation based on the number of decomposing SiC bilayers.

DOI: 10.1103/PhysRevB.80.115433 PACS number(s): 68.37.Ps, 68.37.Ef

I. INTRODUCTION

Graphene, a single layer of carbon sp^2 bonded in a hexagonal lattice, holds great promise for the creation of high-speed electronics.[1] Its experimental discovery, through the use of simple mechanical exfoliation,[2] has spawned a flurry of new research activity. However, the reproducible creation of a uniform graphene film through this method is not practical for large scale manufacturing. One possible route toward manufacturable graphene films is through the thermal decomposition of SiC.[4,5] While this method is reproducible, it has not been able to create a graphene film of uniform thickness.[6–8] At a macroscopic level, the surface progression of SiC to graphene has been readily studied through the use of techniques such as low-energy electron diffraction (LEED) (Refs. 4 and 8) and Raman spectroscopy,[9,10] but understanding of the thermodynamics and kinetics of graphene formation at the surface of SiC is still lacking. There are limited studies on the interesting growth features that occur during the SiC graphitization, especially as imaged by larger area scanning probing microscopy techniques such as atomic force microscopy (AFM).[11,12] Growth features, such as step front erosion, pits, and fingers, cannot be effectively studied with such tools as LEED, Raman spectroscopy, or x-ray photoelectron spectroscopy. These tools provide broad information about the sample surface and the nature of the chemical bonding but not detailed information about localized surface morphology and individual growth features. Therefore, how growth features either help or hinder graphene formation warrants further exploration. For this reason, a systematic approach to the transition of SiC to graphene is taken with the purpose of exploring growth features and their effects on graphene formation.

In this paper, graphene is created on the Si face of 4*H*-SiC through the use of a chemical-vapor deposition (CVD) system. As opposed to systems that solely rely on vacuum conditions, CVD has the benefit of being able to control ambient conditions. Recent explorations of synthesizing graphene in nonultrahigh-vacuum conditions have yielded promising results in controlling film thickness.[13,14] Most studies on graphene creation through elevated heating of SiC have relied on ultrahigh-vacuum conditions.[4,8,11,12,15,16] CVD provides tremendous process flexibility through control of growth time and temperature, chamber pressure, and gas-phase environment. For this study, pressure is fixed in the high-vacuum regime and two variables are altered independently of each other: growth time and temperature. Seven different temperatures and eight different hold times are used with the goal of determining how growth features contribute to, or hinder, the transition from SiC to a continuous film of graphene.

II. EXPERIMENTAL PROCEDURE

The starting substrate material is a 3-inch nominally on-axis, semi-insulating 4*H*-SiC wafer from Cree which is chemomechanically polished on the Si face by NovaSiC. The wafer is diced in-house and wet cleaned in solvent baths followed by a piranha clean ($H_2O_2:H_2SO_4-1:1$) to remove organic contaminants and a buffered oxide etch to remove the native oxide. The samples are immediately loaded into an Epigress VP508 hot-wall CVD system that uses a SiC-coated graphite susceptor. The chamber is roughed out and then filled with hydrogen. Under a controlled chamber pressure and at elevated temperature, a hydrogen environment is used to clean and etch the SiC to obtain a pristine surface. There is no added flux of Si to aid in cleaning or etching. Next, the hydrogen is purged from the chamber and a turbomolecular pump is used to reach a pressure of 1×10^{-6} Torr. The chamber is warmed up to 1100 °C and then ramped at a fixed rate of 10 °C/min to the desired growth temperature for a set amount of time. The pressure in the chamber during

growth is approximately 4×10^{-5} Torr. After high-temperature treatment, the chamber is allowed to cool under high-vacuum conditions. This growth procedure is repeated for each temperature and hold time on a diced piece obtained from the original 3 inch wafer. Each piece is used for only one growth condition and no sample is regrown upon. The temperature of the chamber is measured using a two color Heitronics KT81R pyrometer. Temperature calibration is performed by melting Si in the CVD chamber.

After the chamber cools, the samples are imaged *ex situ* using a Veeco Dimension 3100 AFM in a nitrogen environment at atmospheric pressure. All phase and height data are collected in tapping mode using Veeco microcantilevers. These microcantilevers are uncoated Si with a measured stiffness of 32 N/m, a maximum tip radius of 10 nm (nominal radius is 8 nm), a measured Q factor of approximately 500 and operated at a resonant frequency of 280 ± 15 kHz. The same model of microcantilevers are consistently used to reduce the variability in tapping mode data, such as phase contrast, that is, caused by such factors as cantilever stiffness, tip-sample interaction forces, and tip geometry. Resultant data are analyzed using WSXM.[17]

Scanning tunneling microscopy (STM) measurements are performed under a dry nitrogen environment using a Nanotec Electronica STM.[18] The STM stage is vibration isolated and enclosed in a Faraday cage. Atomically resolved images of highly oriented pyrolytic graphite (HOPG) are used to calibrate the X and Y piezos in accordance with the HOPG atomic lattice constant of 0.246 nm. Similarly, the Z piezo is calibrated using images of surface steps on HOPG and the monostep height of 0.335 nm. The STM tip is mechanically cut from 0.25-mm-diameter PtIr wire. Scans are obtained under constant current mode with tunneling currents, I_{set}, of 0.2–2.4 nA and bias voltages, V_{bias}, of 0.045–1 V. Scans sized between 4×4 nm^2 to 5×5 μm^2 are obtained using scan rates of 1–16 Hz. Nanotec's WSXM scanning probe software (Version 4.0 Develop 13.0) is used to acquire and analyze the STM images.

III. RESULTS AND DISCUSSION

As a starting point for nomenclature and topography analysis, the bulk 4*H*-SiC crystal along the $(11\bar{2}0)$ plane is shown in Fig. 1. The image shows the periodic distance separating SiC bilayers is 0.252 nm. The repeating stacking structure, represented with an *ABC* notation, denotes the rotational differences between the basal planes. The four layers shown in Fig. 1 periodically repeat throughout the bulk crystal; this is the defining characteristic of the 4*H*-SiC polytype. The four layers of the unit cell have a total height of 1.008 nm.

Figure 2 shows a representative AFM image of a hydrogen-etched SiC sample prior to graphitization. The average terrace widths from AFM topography images imply a vicinal angle of 0.1° toward the $\{11\bar{2}0\}$ direction. Further analysis indicates that the mean step height between terraces is 0.493 nm which corresponds to two SiC bilayers.

A. Temperature dependence

The first set of experiments focus on the effect of temperature variation on graphene formation. Each sample has a fixed growth time of 10 min with growth temperatures ranging from 1400 °C to 1600 °C at seven different points.

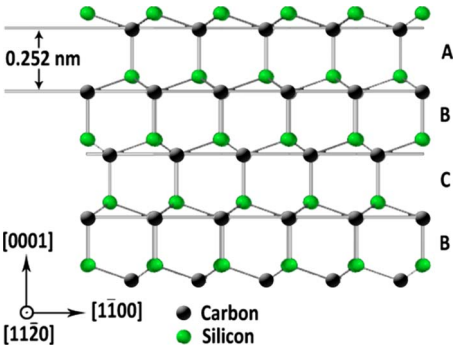

FIG. 1. (Color online) Bulk 4*H*-SiC crystallographic structure along the $(11\bar{2}0)$ plane. The horizontal lines cutting across the carbon atoms are guides representing the periodic spacing between bilayers. The repeating *ABC* letters represent the periodic stacking structure unique to the 4*H*-SiC polytype.

At 1400 °C the surface is characterized by roughened SiC step faces and signs of macroscale step bunching. The terraces are no longer monotonically changing by two SiC bilayers as exhibited in Fig. 2. Instead, the surface is characterized by step height differences in multiples of 0.5 nm. This deviation from monotonic step heights suggests that some steps are more prone to erode and bunch. Figure 3 shows AFM topography data from the surface of a 1400 °C sample. As can be seen, most terraces are a multiple of 0.5 nm above the reference height. Only one partial terrace present in Fig. 3 does not follow this trend. This terrace is 1.25 nm above the reference height. Compared to the other terraces, this one has the smallest surface area; it appears to be eroding from both the front and rear. This demonstrates that terraces do not erode solely in a reverse step-flow growth manner. Under a reverse step-flow growth, the erosion would occur only from the front of the terraces and all terraces would erode in a lock-step manner. However, the 1.25 nm terrace refutes that erosion only occurs from the front of the terrace and it being a nonmonotonic step height

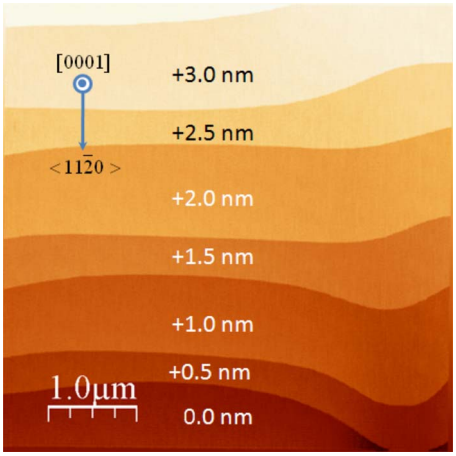

FIG. 2. (Color online) Topographic AFM image of 4*H*-SiC surface after hydrogen etching at 1500 °C for 10 min. Data has been locally plane fit to highlight the terrace step height.

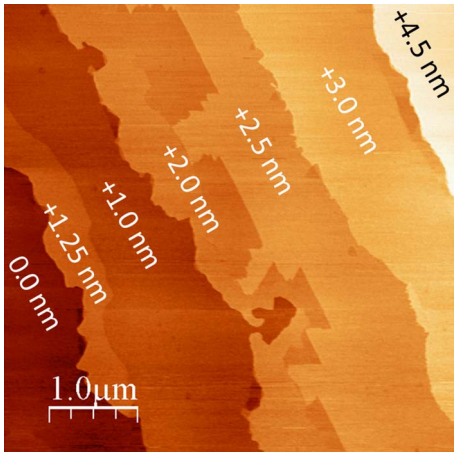

FIG. 3. (Color online) Topography AFM image of 4*H*-SiC surface after exposure to 1400 °C for 10 min in high-vacuum. Phase measurements from AFM show no graphene on the surface. Data has been locally plane fit to better show height variations between terraces.

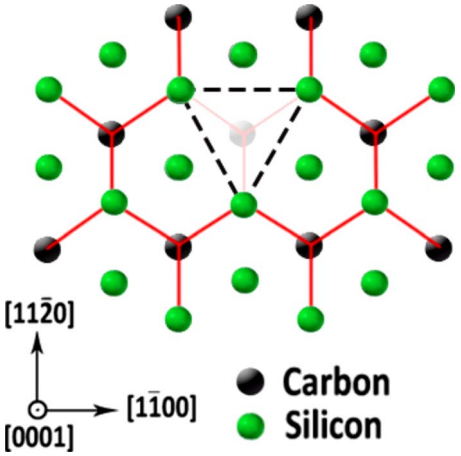

FIG. 4. (Color online) The basal plane of an unreconstructed Si face 4*H*-SiC surface is shown with solid lines representing the sp^3 bonds characteristic of SiC. A point defect caused by the vacancy of a carbon atom is outlined by the dashes. This vacancy lowers the number of bonds along the $\{11\bar{2}0\}$ planes which are represented by the dashed triangle.

suggests that some terraces are more prone to erosion than others.

The unequal erosion is attributed to terraces having different surface energies.[11] Variation in surface energy has been found by Kimoto and cited as a probable cause of macroscopic step bunching.[19] The stacking sequence of the relative basal plane below the surface determines the erosion rate for the surface bilayer. The stacking sequence with the lowest surface energy will be the most prevalent on the surface. In the case of 4*H*-SiC(0001), the stacking sequence leads to the formation of steps with height multiples of two bilayers instead of a single bilayer. This is the phenomenon depicted in Fig. 3. Higher surface energy terraces have disappeared through their erosion into the terraces with slower erosion rates. This creates the nonmonotonic change in the step heights between terraces.

1. Formation of terrace pits

In addition to terrace erosion at 1400 °C, pits begin to form on the terrace surface. These initial pits are not the same as those found by Hannon *et al.*[11] Unlike the step-edge pits found by Hannon *et al.*, these initial pits form on the terrace itself away from any step front suggesting that their cause is not from a retracting step front. Two possible reasons for pit formation are point defects and dislocations in the SiC bulk.[9] If dislocations in the bulk were the sole cause of pit formation, then an increase in growth temperature should not cause an increase in pit density and the number of dislocations spread across the SiC substrate should be approximately uniform. However, if the density of pits shows a clear trend of increasing with temperature, then point defects are a more likely cause. The fraction of a surface covered by point defects exponentially increases with temperature as given by

$$f = e^{-E_v/k_B T}, \tag{1}$$

where k_B is Boltzmann's constant, T is temperature, and E_v is the required energy for an atom to create a surface vacancy.[20]

Topography data from AFM are used empirically with this equation in an attempt to explain the origins of the pits. The number of discernible terrace pits are counted across multiple 5×5 μm^2 AFM topography scans to determine pit density. At 1400 °C there is an average density of 0.49 μm^{-2} pits and at 1450 °C the average density is 0.76 μm^{-2}. Above this temperature the pit density becomes difficult to estimate given the severe morphological changes that are occurring on the surface. If dislocations arising from the bulk and terminating on the surface, such as threading or edge dislocations, were the sole cause of terrace pit formation, then there should not be such a significant change in density with an increase in temperature. There should be relatively similar numbers of these dislocations given that all samples were cut from the same wafer and counting defects across multiple AFM scans should average out statistical inconsistencies. However, this is not found to be the case. There is a 55 percent increase in the number of terrace pits for a 50 °C increase in growth temperature. Using this rise in temperature and the increase in pit density, Eq. (1) estimates that the energy to form a vacancy should be approximately 2.2 eV. This simple calculation based on only two data points is not far from simulation values of 2.7 eV for the creation of a C vacancy.[21] Furthermore, Gao *et al.*[21] have shown through molecular-dynamic simulations that the formation of a C vacancy requires less energy as compared to creating a Si vacancy. This simulation suggests that it is more likely for a C atom to be vacant as compared to a Si atom. To illustrate the effect of a point defect, Fig. 4 shows a C vacancy on an unreconstructed Si face surface. The vacant atom is highlighted with the dashed lines. The removal of the C atom creates reduced bonding sites along the $\{11\bar{2}0\}$ planes.

To further explore pits, a sample prepared at 1475 °C is analyzed with STM. A pit that is approximately 1.0 nm below the terrace surface is imaged in Fig. 5. From data analysis of Fig. 5(a), the pit rms roughness is five times greater

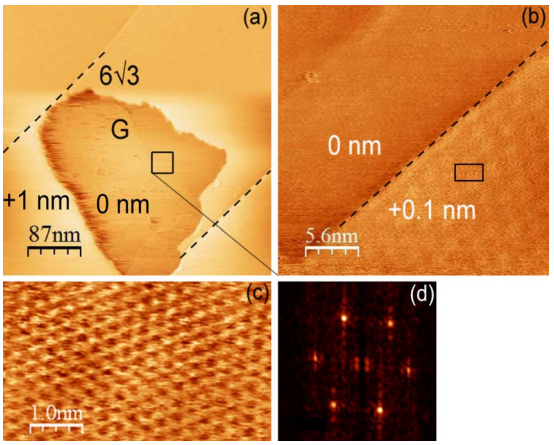

FIG. 5. (Color online) Terrace pit on a 1475 °C, 10 min hold time, sample imaged with STM. The bottom of the pit is covered in graphene, denoted G in (a). As shown in (b), further magnification into the pit reveals subtle topographic structure with crystallographic preference parallel to step fronts in (a), that is, highlighted with dashed lines. The image depicted in (c) is taken from scanning the rectangular area highlighted in (b). A 2D-FFT of (c) exhibits an atomic lattice with periodicity of 0.249 ± 0.01 nm as shown in (d). The accepted lattice periodicity for graphene is 0.246 nm. Scanning parameters for these data are I_{set}=0.22 nA and V_{bias}=0.25 V.

than the terrace rms roughness. At the bottom of the pit, as shown in Fig. 5(b), is an atomic step, that is, parallel to the taller terraces in Fig. 5(a) as demarcated by dashed lines. This step is not tall enough to be a SiC bilayer (0.252 nm) or a graphene monolayer (0.335 nm), but it still shows clear preference for erosion along the same crystallographic direction. Such steps have been shown by Huang *et al.*[22] to be the effect of the height differences between a top layer of graphene blanketing the underlying reconstructed SiC layer and another layer of graphene. An atomic scale image of the pit bottom is shown in Fig. 5(c). A two-dimensional fast Fourier transform (2D-FFT) of the data reveals a hexagonal atomic structure with a lattice constant of 0.249 ± 0.01 nm close to the lattice constant for graphene of 0.246 nm. Thus, graphene covers the bottom of the pit.

The majority of terrace pits, especially as they increase in size, show a clear crystallographic preference which they form along. This preference is exhibited by eroding terraces as well. The mechanism that drives pit erosion appears to be the same for terrace erosion. This phenomenon is seen in Fig. 6. Topographic AFM data shows that both the pits and the terraces erode along the threefold symmetric $\{11\bar{2}0\}$ planes demonstrating a preference for erosion along these low-index crystallographic planes. From the analysis of the point-defect formation, these planes have reduced bonding sites due to vacancies promoting parallel erosion along the $\{11\bar{2}0\}$ crystallographic directions.

The pits also confirm the stoichiometric requirement that at least three SiC bilayers are needed to create a single monolayer of graphene.[3,5] As seen in the topographic AFM image in Fig. 7(a), two pits have formed. Both pits are next to one another on the same terrace, have opened along the $\{11\bar{2}0\}$ planes, and are of similar area. The difference be-

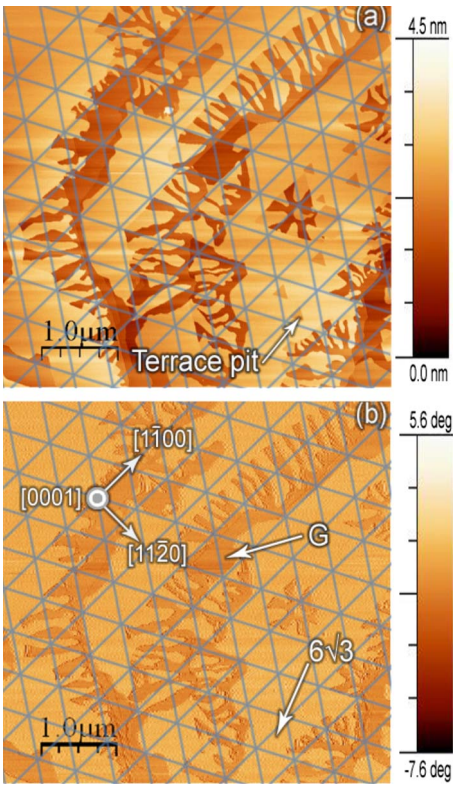

FIG. 6. (Color online) Images of AFM (a) topography and (b) phase of a 1475 °C sample held at temperature for 10 min showing preference for erosion of steps and terrace pits along the $\{11\bar{2}0\}$ planes. Reference grid is overlaid to guide the eye along the $\{11\bar{2}0\}$ set of planes. Phase contrast in (b) demarcates regions of graphene, labeled as G, and regions of reconstructed SiC.

tween the two pits is that one pit, as shown in Fig. 7(b), has a depth of 0.5 nm and the other pit, shown in Fig. 7(c), has a depth of 1.0 nm. Figure 7(d) is a phase AFM image showing that the 0.5-nm-deep pit exhibits no phase contrast, which is magnified in Fig. 7(e), while the 1.0-nm-deep pit shows a distinct and uniform phase contrast between the terrace top and the pit bottom in Fig. 7(f). With only two bilayers decomposed in the 0.5 nm pit, there should be enough carbon to cover at least 62.6 percent of the pit bottom with graphene. However, this potential graphene coverage is not reflected in the phase image. With four SiC bilayers collapsing to form the 1.0 nm pit, there is a uniform and measurable phase contrast at the bottom of the pit. As phase contrast is sensitive to material properties, this contrast suggests that the 1.0 nm pit and terraces are composed of different materials. The example shown in Fig. 7 is not an isolated event. The same relationship between phase contrast and pit depth is exhibited on other regions of this sample as well as on other samples grown at 1475 °C. Additionally, the area of the pit does not appear to play a role, only the depth of the pit.

The STM data of Fig. 5 corroborates well with the AFM data of Fig. 7. A 1.0-nm-deep pit shows definitive signs of graphene on its bottom which corresponds to the AFM data showing a phase contrast for the 1.0 nm pit in Fig. 7(f). A graphitic phase contrast is first noticed at a temperature of 1450 °C. This suggests that there are two materials present

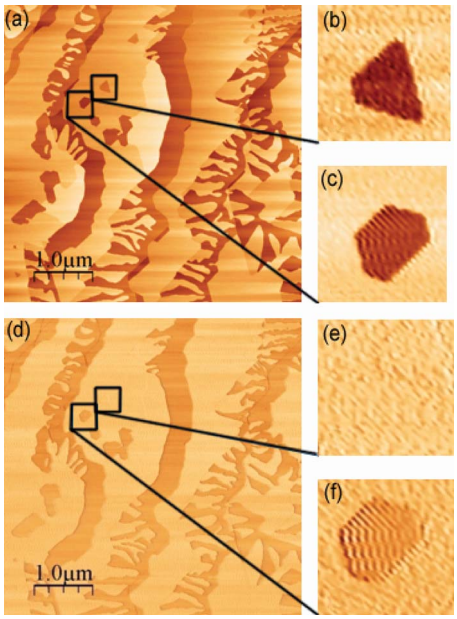

FIG. 7. (Color online) (a) Two terrace pits are highlighted on the AFM topography image, (b) one that is 0.5 nm deep and (c) a second that is 1.0 nm deep. (d) From AFM phase analysis, (e) the 0.5 nm pit does not show phase contrast indicating that the pit and terrace are the same material; (f) only the 1.0-nm-deep pit shows signs of phase contrast. Imaged sample surface grown at 1475 °C with 10 min hold time.

on the surface, one that comprises of the terrace surface and one that has collapsed into graphene. Further analysis of phase contrast will be elaborated on later in this paper.

At the onset of graphitization, no raised islands of either graphene or reconstructed SiC buffer layer are found on the surface of the terraces.[11] Topography images from AFM show the only features on the terraces themselves to be pits not islands. The reason behind the different surface morphologies lies in the experimental parameter space. This work operates in a different pressure, and necessarily higher temperature, regime as compared to ultrahigh-vacuum studies. The phase transformation and surface morphology dependence on background growth pressure versus temperature has been studied by Tromp *et al.*[13]

2. Formation of fingers

Above 1450 °C growth features other than pits become apparent. The formation of "fingers" begins. These fingerlike structures of SiC form perpendicular to an eroding SiC step front. A step front can be formed by either terrace faces or pit faces. Figure 8 shows the surface morphology at 1475 °C with well-defined finger structures. Topographic AFM analysis reveals that the surface of the fingers is on average 0.2 nm below the surface of their originating terrace. In other words, the fingers refer to the elevated structures that are 0.8 nm above the reference height. Between the fingers, as depicted in Fig. 8 as the 0 nm reference height, is an area that will be referred to as the depressed interdigitated region. The fingers do not emanate solely from erosion at intrinsic SiC step edges. They can also form inside pits that are at least 1.0 nm deep.

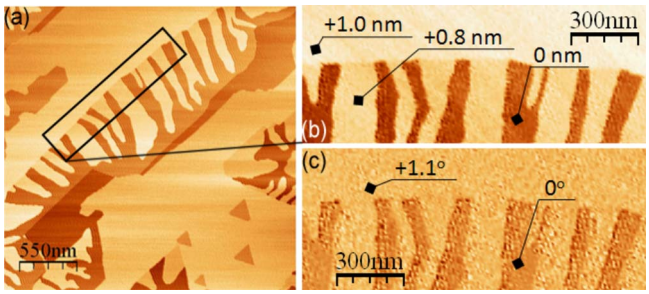

FIG. 8. (Color online) (a) Topographic AFM image showing finger structure after graphitization at 1475 °C for 10 min. Magnification of (b) topography and (c) phase data are shown in the insets. The features 0.8 nm above the reference height in (b) are referred to as "fingers" and the reference height is referred to as a "depressed interdigitated" region. Inset topography image has been locally plane fit to better show height variation between surface features.

Figure 6(a) shows two terrace pits that have eroded sufficiently for fingers to form within them. These fingers emanate from both the vertices and midpoint of the triangular pit and point toward the center of the triangular pits, as seen in Fig. 6. This similarity between pits suggests that the mechanism driving finger formation is not a random occurrence. It also provides further evidence that the erosion of terrace pits happens in the same manner as erosion of SiC terraces. The step fronts of both pits and terraces erode along the same crystallographic planes and can give rise to finger formation.

To study the fingers further, Fig. 9(a) shows an STM image analyzing the surface composition of a finger and terrace. A 2D-FFT of these surfaces in Fig. 9(b) reveals a hexagonal

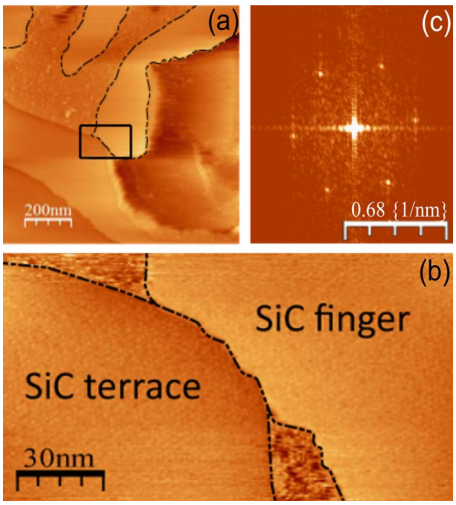

FIG. 9. (Color online) Image of STM data from a 1475 °C, 10 min hold time, sample showing (a) outlined finger structures on the surface with the associated depressed interdigitated regions and (b) a magnified image of the rectangular region in (a) showing a detailed SiC surface reconstruction. A 2D-FFT of the SiC finger region of (b) reveals a hexagonal structure in (c) with a lattice spacing of 1.91 ± 0.01 nm. A 2D-FFT of the SiC terrace is very similar to (c) with a lattice spacing value of 1.89 ± 0.01 nm. Scanning parameters for these data are $I_{set}=0.2$ nA and $V_{bias}=1.0$ V.

structure shown in Fig. 9(c). The 2D-FFT for both the terrace and finger regions are very similar. The 2D-FFT measured lattice periodicity for the SiC finger shown in Fig. 9(b) is 1.91 ± 0.01 nm. Similarly, the SiC terrace is found to have a periodicity of 1.89 ± 0.01 nm. These calculations are close to the 6×6 periodicity observed by STM for a C-rich reconstructed SiC buffer layer.[12,23] The fingers themselves are relatively smooth, with an average rms roughness of 0.08 nm, as compared to the depressed interdigitated regions between the fingers, which have an average rms roughness of 0.4 nm. STM scans of monolayer and bilayer graphene films on SiC(0001) show an interface-induced roughness.[12,24] In the rough depressed interdigitated regions, few-nm diameter clusters of atoms were also observed by STM. Stochiometric analysis suggests that these clusters are excess surface carbon that has either not formed a layer of graphene or is in excess of the quantity needed for a C-rich buffer layer. Scanning over these clusters with an STM tip frequently resulted in clusters adhered to the STM tip and caused difficulty in obtaining atomic resolution in the depressed interdigitated regions. Further increases in temperature or hold time enable this excess carbon to form graphene layers and reduce surface roughness.[24]

Corroborating with STM data allows for regions in AFM scans to be defined by their phase contrast. An example of how contrast is used to demarcate regions is shown in Fig. 6(b). The average contrast difference between the two regions is approximately 1.9°. The fingers do not show phase contrast compared to the terraces from which they emanate; this confirms the STM finding that both the fingers and terraces are the same material. Furthermore, STM scans showing that the depressed interdigitated regions are not reconstructed SiC supports the phase contrast seen between the fingers, as seen in Fig. 8(c). The phase contrast suggests that the terraces and fingers are reconstructed SiC while the depressed interdigitated regions are graphene. The practicality of AFM tapping mode to detect material differences is extended further in determining the relative surface coverage of graphene.

Using Fig. 8 as a representative example, an analysis of just the finger region reveals that the depressed interdigitated area makes up 62 percent of the finger region. Assuming only graphene exists in the depressed interdigitated area and calculating the number of carbon atoms required to form a monolayer, only two bilayers of SiC are needed to produce sufficient carbon for this region. However, the finger structures have been found to be raised at least three SiC bilayers above the graphene surface. From a stoichiometric point of view, erosion of slightly more than three SiC bilayers provides sufficient carbon to create a continuous monolayer film of graphene.[3,5] However, continuous graphene is not seen at this temperature. The fingers serve as a barrier preventing continuous graphene formation. Even though coherent graphene has been found to blanket steps,[15,16,18] these fingers do not show signs of graphene coverage. They hinder the formation of continuous graphene.

As temperature increases above 1450 °C, the fingers continue to lengthen until the step front they originated from has completely eroded away. A terrace with fingers can either erode into another terrace with a slower erosion rate or the terrace itself can erode from its back toward the step front. The terraces themselves have a different erosion rate as compared to the fingers despite both having the same reconstructed SiC surface. This erosion rate difference is attributed to the one SiC bilayer step down from terrace surface to finger surface as shown in Fig. 8(b). A SiC bilayer step changes the stacking sequence terminating on the surface which affects the surface energy as previously discussed. Once the step front completely erodes, the fingers become SiC islands.

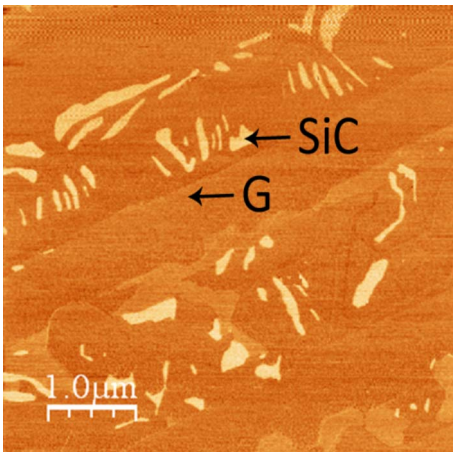

FIG. 10. (Color online) Phase AFM image showing SiC islands on a mostly graphitized surface at 1550 °C.

Figure 10 shows a phase AFM image that exhibits these SiC islands as remnants on a mostly graphitized surface at 1550 °C. Atomic-resolution STM scans (not shown) at 1550 °C confirm the presence of a graphene overlayer covering the regions between the SiC islands. With further increases in temperature, these islands begin to shrink in size approaching the point where the surface is completely covered by graphene. These islands are the last growth feature to overcome before a continuous graphene film forms.

3. Phase analysis of surface conversion

Contrast in the phase data of AFM is used to track the dependence of surface composition on changing growth conditions. Assuming that there are only two materials on the surface of the samples, reconstructed SiC and graphene, the relative surface area of each material can be tracked via AFM phase analysis. To this end, an approximate surface coverage fraction can be extracted and plotted. Using a histogram analysis, the phase information of each and all AFM images is captured individually. The resulting individual histogram data is well represented with a fit to two normal curves, one for graphene and one for SiC. The area under each fitted normal curve is calculated and the surface coverage percentage is determined as

$$\%_{\mathrm{G}} = \frac{A_{\mathrm{G}}}{A_{\mathrm{G}} + A_{\mathrm{SiC}}}, \tag{2}$$

$$\%_{\mathrm{SiC}} = 1 - \%_{\mathrm{G}}, \tag{3}$$

where A_{G} is the area under the graphene portion of the normal curve and A_{SiC} is the area of SiC. The relative percent-

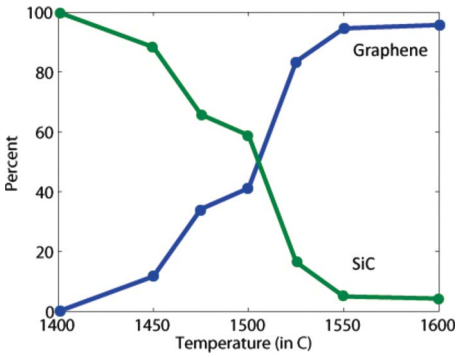

FIG. 11. (Color online) Surface coverage of graphene and SiC as a function of growth temperature with growth time kept constant at 10 min.

ages of SiC as compared to graphene are captured by $\%_{SiC}$ and $\%_G$, respectively. For each growth condition, all the individually calculated areas are then averaged together. These averaged percentages have been compiled and plotted against temperature which is shown in Fig. 11. It is shown that graphene surface coverage is a function of temperature. This plot does not relate the thickness or number of graphene layers to the growth temperature; it is only a measure of surface coverage. At temperatures above 1500 °C, with a hold time of 10 min, the surface is covered by more than 50 percent graphene. The excess surface carbon in between the SiC fingers at lower growth temperature has a very similar phase contrast compared to graphene. Since its phase is indistinguishable from graphene, any excess surface carbon serves to increase the variance of the averaged data in Fig. 11. At higher growth temperatures this added variance is lessened with the decrease in excess surface carbon.

This changing surface composition is reflected in the overall surface morphology. As temperatures rise above 1500 °C the surface morphology smoothes out with a lower density of high aspect ratio features such as fingers and pits. As graphitization progresses at higher temperatures, the surface becomes blanketed with continuous graphene. There are few remnants of the finger structures remaining. Previous studies have shown that continuous layers of graphene blanket surface features such as terrace steps.[15,16,18] At the highest temperature point studied, 1600 °C, the surface has a continuous graphene film that continues to show strong crystallographic preference through its well-faceted features. This is demonstrated in the AFM images of Fig. 12.

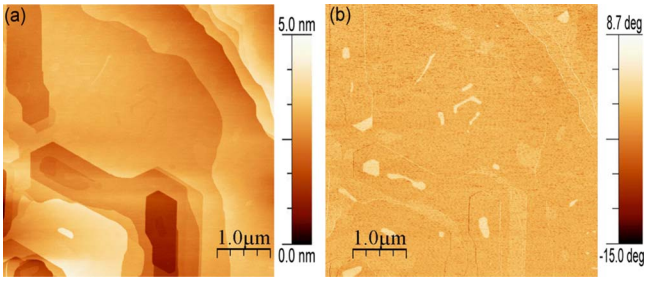

FIG. 12. (Color online) (a) Topographic and (b) phase AFM image of 1600 °C sample showing a well-faceted graphitized surface.

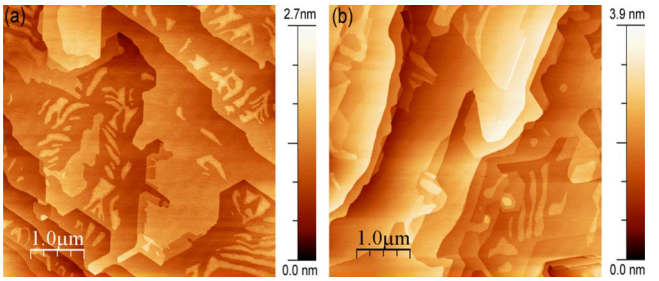

FIG. 13. (Color online) Topographic AFM images of (a) 30 min and (b) 60 min samples prepared at 1475 °C.

B. Time dependence

The second set of experiments focused on varying time instead of temperature to create graphene. The temperature chosen was 1475 °C because it was found to have a partially graphitized surface at a growth time of 10 min. The time-dependent experiments range from 0 to 60 min at eight different points.

The formation mechanisms and features that are seen in the temperature-dependent experiments are prevalent in the time-dependent experiments as well. The formation of graphene, from a growth feature standpoint, occurs in the same way as noted for temperature dependence. At 0 min, there is macroscale step bunching. At 2 min through 14 min, fingers begin to form and lengthen. At 16 min, the SiC fingers are detached from their step fronts and become islands. As time increases further, the sharp pit and finger features are smoothed with graphene blanketing the surface. Topography AFM images from both 30 and 60 min growth times are seen in Fig. 13. As seen in Fig. 13(a), the 30 min sample still contains reconstructed SiC islands. The distance between the nearest edge of these islands and the eroded step front from which the fingers emanated is approximately the same for every island. This suggests that the islands are remnants of step fronts with equal erosion rates. Increasing time to 60 min, Fig. 13(b) shows a surface, that is, nearly covered by a continuous film of graphene. All but a few of the SiC islands remain. Throughout the entire graphitization, the same well-faceted surface features are exhibited. By varying either the graphitization time or temperature it is found that the graphene formation mechanism is the same.

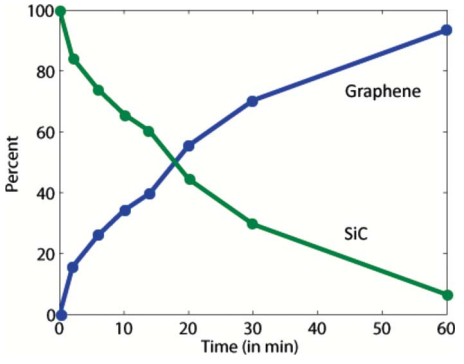

FIG. 14. (Color online) Surface coverage of graphene and SiC as a function of hold time with hold temperature kept constant at 1475 °C.

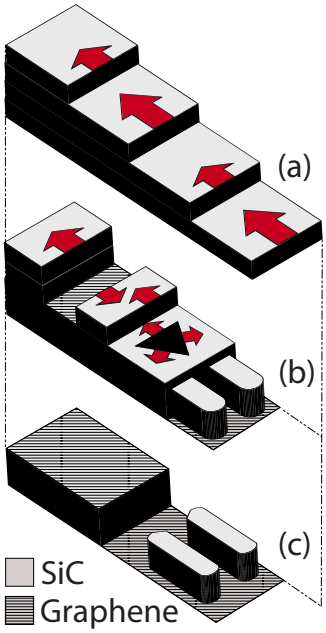

FIG. 15. (Color online) Progression of a 4*H*-SiC(0001) surface toward graphene as envisaged through growth features. (a) Hydrogen etched SiC surface showing monotonic two SiC bilayer steps with arrows representing relative erosion rates due to basal plane stacking sequence. Longer arrows represent faster erosion rates. (b) Surface morphology that is likened to a 1475 °C sample with three distinct features. First, macroscale step bunching has occurred with fingers emanating from the step-bunched terrace. Second, a terrace pit has opened along the $\{11\bar{2}0\}$ planes. Third, terraces do not erode solely in a reverse step-flow growth manner. (c) Surface morphology that is likened to a 1550 °C sample. Further terrace and pit erosion lead to a higher surface coverage of graphene. Islands of reconstructed SiC left from fingers are a barrier for continuous graphene.

As with the temperature-dependent study, the surface coverage of graphene as a function of time is studied through AFM phase analysis. Using the same methods described previously, a plot of the relative coverage of graphene across the surface as a function of hold time is seen in Fig. 14. As growth hold time increases so does the coverage of graphene on the surface. The surface required more than 14 min to become half covered with graphene.

IV. CONCLUSION

The dependence of time and temperature on graphene synthesis on the Si face of 4*H*-SiC is studied. The surface conversion toward a continuous graphene film is demonstrated by AFM and STM. It is found that the same surface growth features emerge in both time and temperature experiments. First, macroscopic step bunching in multiples of two SiC bilayers occurs through unequal terrace erosion. This is due to surface energy differences created by the SiC basal plane stacking sequence. Further terrace erosion leads to the creation of fingers that form perpendicular to the step front. These elevated fingers are reconstructed SiC with graphene found in the depressed interdigitated region between them. At higher temperatures, or longer growth times, these fingers form islands which disappear and leave behind a smooth surface blanketed with graphene. The fingers are the last growth feature to overcome before a continuous graphene film is formed and are a hindrance to graphene formation. Figure 15 highlights the graphitization process.

Throughout the entire graphene synthesis, surface features are well-faceted with a strong crystallographic preference along the $\{11\bar{2}0\}$ planes. These features include pit formations and terrace erosion. Pit density shows a tendency to increase with temperature indicating point defects, and not dislocations alone, play a role in nucleating the pits. Once formed, these pits erode in the same manner as the terraces themselves.

ACKNOWLEDGMENTS

This work is supported by DARPA, the Air Force Research Laboratories, and Indiana 21st Century Fund.

*mbolen@purdue.edu
†Present address: Sandia National Laboratories, Albuquerque, NM 87185.

[1] Y. Q. Wu, P. D. Ye, M. A. Capano, Y. Xuan, Y. Sui, M. Qi, J. A. Cooper, T. Shen, D. Pandey, G. Prakash, and R. Reifenberger, Appl. Phys. Lett. **92**, 092102 (2008).
[2] K. S. Novoselov, A. K. Geim, S. V. Morozov, D. Jiang, Y. Zhang, S. V. Dubonos, I. V. Grigorieva, and A. A. Firsov, Science **306**, 666 (2004).
[3] J. Hass, W. A. de Heer, and E. H. Conrad, J. Phys.: Condens. Matter **20**, 323202 (2008).
[4] E. Rollings, G.-H. Gweon, S. Y. Zhou, B. S. Mun, J. L. McChesney, B. S. Hussain, A. V. Fedorov, P. N. First, W. A. de Heer, and A. Lanzara, J. Phys. Chem. Solids **67**, 2172 (2006).
[5] A. Van Bommel, J. Crombeen, and A. Van Tooren, Surf. Sci. **48**, 463 (1975).
[6] T. Ohta, F. El Gabaly, A. Bostwick, J. L. McChesney, K. V. Emtsev, A. K. Schmid, T. Seyller, K. Horn, and E. Rotenberg, New J. Phys. **10**, 023034 (2008).
[7] H. Hibino, H. Kageshima, F. Maeda, M. Nagase, Y. Kobayashi, and H. Yamaguchi, Phys. Rev. B **77**, 075413 (2008).
[8] C. Berger, Z. Song, T. Li, X. Li, A. Ogbazghi, R. Feng, Z. Dai, A. Marchenkov, E. Conrad, P. First, and Walt A. de Heer, J. Phys. Chem. B **108**, 19912 (2004).
[9] N. Camara, G. Rius, J. Huntzinger, A. Tiberj, L. Magaud, N. Mestres, P. Godignon, and J. Camassel, Appl. Phys. Lett. **93**, 263102 (2008).
[10] Z. H. Ni, W. Chen, X. F. Fan, J. L. Kuo, T. Yu, A. T. S. Wee, and Z. X. Shen, Phys. Rev. B **77**, 115416 (2008).
[11] J. B. Hannon and R. M. Tromp, Phys. Rev. B **77**, 241404(R) (2008).
[12] C. Riedl, U. Starke, J. Bernhardt, M. Franke, and K. Heinz,

Phys. Rev. B **76**, 245406 (2007).
[13] R. M. Tromp and J. B. Hannon, Phys. Rev. Lett. **102**, 106104 (2009).
[14] K. V. Emtsev, A. Bostwick, K. Horn, J. Jobst, G. L. Kellogg, L. Ley, J. L. Mcchesney, T. Ohta, S. A. Reshanov, J. Rohrl, Eli Rotenberg, Andreas K. Schmid, Daniel Waldmann, Heiko B. Weber, and Thomas Seyller, Nature Mater. **8**, 203 (2009).
[15] T. Seyller, K. Emtsev, K. Gao, F. Speck, L. Ley, A. Tadich, L. Broekman, J. Riley, R. Leckey, O. Rader, A. Varykhalov, and A. M. Shikin, Surf. Sci. **600**, 3906 (2006).
[16] G. Rutter, J. Crain, N. Guisinger, P. First, and J. Stroscio, J. Vac. Sci. Technol. A **26**, 938 (2008).
[17] I. Horcas, R. Fernandez, J. Gomez-Rodriguez, J. Colchero, J. Gomez-Herrero, and A. Baro, Rev. Sci. Instrum. **78**, 013705 (2007).
[18] L. B. Biedermann, M. L. Bolen, M. A. Capano, D. Zemlyanov, and R. G. Reifenberger, Phys. Rev. B **79**, 125411 (2009).
[19] T. Kimoto, A. Itoh, H. Matsunami, and T. Okano, J. Appl. Phys. **81**, 3494 (1997).
[20] M. Ohring, *Materials Science of Thin Films: Deposition and Structure*, 2nd ed. (Academic, New York, 2002).
[21] F. Gao, M. Posselt, V. Belko, Y. Zhang, and W. J. Weber, Nucl. Instrum. Methods Phys. Res. B **218**, 74 (2004).
[22] H. Huang, W. Chen, S. Chen, and A. T. S. Wee, ACS Nano **2**, 2513 (2008).
[23] W. Chen, H. Xu, L. Liu, X. Gao, D. Qi, G. Peng, S. Tan, Y. Feng, K. Loh, and A. Wee, Surf. Sci. **596**, 176 (2005).
[24] P. Lauffer, K. V. Emtsev, R. Graupner, T. Seyller, L. Ley, S. A. Reshanov, and H. B. Weber, Phys. Rev. B **77**, 155426 (2008).